Solid-to-plasma transition of polystyrene induced by a nanosecond laser pulse within the context of inertial confinement fusion

R. Liotard,[1] B. Canaud,[2] A. Pineau,[3] A. Sollier,[2] E. Lescoute,[2] A. Colaïtis,[1] and G. Duchateau[4]

[1]*University of Bordeaux-CNRS-CEA, CELIA, 33400 Talence, France*

[2]*Université Paris-Saclay, CEA, LMCE, F-91680 Bruyères-le-Châtel, France and CEA, DAM, DIF, F-91297 Arpajon, France*

[3]*Laboratory for Laser Energetics, University of Rochester, 250 East River Road, Rochester, New York 14623, USA*

[4]*CEA-CESTA, 15 Avenue des Sablières, CS 60001 F-33116 Le Barp Cedex, France*

(Received 27 November 2023; accepted 1 April 2024; published 12 June 2024)

Laser direct drive (LDD) inertial confinement fusion (ICF) involves irradiating a spherical target of thermonuclear fuel coated with an ablator, usually made of polystyrene. Laser energy absorption near the target surface leads to matter ablation, hydrodynamic shocks, and ultimately capsule implosion. The conservation of spherical symmetry is crucial for implosion efficiency, yet spatial modulations in laser intensity can induce nonuniformities, causing the laser imprint phenomenon. Understanding laser imprint, especially considering the initial solid state, is essential for advancing LDD ICF. A first microscopic model of solid-to-plasma transition was built in 2019, accounting for laser absorption in the solid state with a band-structure-based ionization model. This model has been improved to include chemical fragmentation and a more accurate description of electron collision frequency in various matter states. The latest development involves assessing the model's reliability by comparing theoretical predictions with experimental observations. Despite the success of this approach, questions remain, leading to further investigations and observations under different irradiation conditions. This work presents an experiment with a nanosecond pulse, taking into account hydrodynamic effects, and measures transmission dynamics over the entire laser beam area to observe two-dimensional effects. The objective is to adapt the theoretical model, couple it with a hydrodynamic code, and observe additional effects related to the initial solid state.

DOI: 10.1103/PhysRevE.109.065207

I. INTRODUCTION

Laser direct drive (LDD) inertial confinement fusion (ICF) consists in irradiating a spherical target of thermonuclear fuel (deuterium and tritium) possibly coated by a plastic (polystyrene, CH) ablator [1]. The laser energy is absorbed in the vicinity of the target surface, leading to matter ablation, the formation of hydrodynamic shocks, and subsequent capsule implosion through the so-called rocket effect [2]. The implosion is expected to drive the matter in extreme conditions activating fusion reactions of deuterium and tritium. The efficiency of this process relies on the conservation of the spherical symmetry over the course of the implosion. The irradiation is thus performed through a set of symmetrically arranged overlapping laser beams. Due to limitations of the laser facilities, the total laser intensity exhibits speckles and nonuniformity at different spatial scales, departing from the spherical symmetry of irradiation. Such spatial perturbations of the laser incident intensity induce a nonuniform ablation of the target, leading to a modulated ablation surface and rippled shocks. The latter process is the so-called laser imprint [3]. These ablation surface modulations can be exponentially enhanced through the Rayleigh-Taylor instability during the target acceleration, leading to strong deviations from the symmetrical implosion and subsequent decrease in the efficiency of the ICF scheme. Experimental results have shown that the initial solid state of the target can enhance the nonuniformity of ablation and shocks [4,5]. This enhancement has been shown to be due to the nonlinear laser absorption taking place in the solid state. Despite the fact that the plasma state is the main matter phase in ICF, the previous observation suggests that the initial solid state also plays a role in the laser imprint process, and thus it may affect the ICF efficiency. Therefore, understanding the laser imprint process including the initial solid state is crucial for the development of LDD ICF.

In addition to experimental investigations such as those carried out on large laser facilities, theoretical and numerical efforts allow one to progress in the understanding of the above-mentioned processes. Since most of the current state-of-the-art numerical codes enabling us to perform radiative-hydrodynamics simulations do not include the laser-induced transition of the ablator from the solid state to the plasma state, there is a need to develop a simple and reliable model describing this transition so that it can be implemented in the numerical codes. Such a theoretical work has been launched over the past few years. A first attempt of microscopic modeling accounting for the laser absorption in the solid state, and describing the solid-to-plasma transition, was developed in 2019 [6]. By including the electron band structure of the material, including in particular the band gap characterizing dielectrics as polystyrene, the photoionization and impact ionization were properly described through quantum calculations, allowing us to simulate the evolution of the free-electron density from zero to the critical value, i.e., from the initial insulating solid to a plasma state. By evaluating

the absorption of the produced free electrons with a Drude model, its coupling with a two-temperature (of electrons and lattice) model allows us to predict the phase transitions. Since the free-electron production is driven by two-photon absorption, numerical simulations confirm the expected nonlinear behavior of the absorption with respect to the laser intensity. It was also shown numerically that the timescale for the solid-to-plasma transition is of the order of 100 ps, which is of the same order of magnitude as an ICF picket duration, confirming the expected role of the initial solid state. Another confirmation has been obtained by implementing this model in a one-dimensional hydrocode, showing that the dynamics of shock waves is modified by the initial solid state [7]. Although this first microscopic modeling laid the foundations of the description of the solid-to-plasma transition, it has been improved by including the chemical fragmentation of the polystyrene ablator and better describing the electron collision frequency in various matter states [8,9]. The last stage of such developments is assessing their reliability by comparing theoretical predictions to experimental observations. Such an approach has recently been initiated by carrying out a dedicated table-top experiment based on the transient transmission of CH foils [10]. Indeed, it is related to the solid-to-plasma transition since the foil is initially transparent and becomes opaque when the plasma forms. The transmittance, i.e., the ratio of transmitted laser intensity to incident laser intensity, then drops from unity to zero. This experiment involved exposure of CH foils to a laser pulse exhibiting the characteristics of ICF pickets, i.e., 100 ps pulse duration and 355 nm wavelength. The transient transmission was obtained with a 250 fs probe pulse that enabled acquisition of time-resolved images of the plasma formation process. By coupling the above-mentioned solid-to-plasma transition model to a description of laser propagation (resolution of the one-dimensional Helmholtz equation), the transmission dynamics has been evaluated and compared with experimental observations. Both were shown to be in good agreement, first providing a validation of theoretical developments for their subsequent introduction in three-dimensional hydrocodes designed for ICF.

Despite the success of such an approach, some questions remain due to assumptions made in the previous study and the possibility of carrying out additional observations, possibly exhibiting supplemental physical processes. More generally, to check the reliability of the theoretical developments in other irradiation conditions is a second step of the whole approach. It may further validate the solid-to-plasma model and exhibit additional physical processes related to the initial solid state. In the above-mentioned experiment [10], a 100 ps pulse duration was used, allowing us to neglect the hydrodynamic effects over the course of laser-matter interaction, and the temporal evolution of the foil transmission was measured only in the center of the pump laser beam, avoiding possible two-dimensional or three-dimensional effects. Additional information is thus expected by irradiating a plastic foil with a nanosecond pulse (hydrodynamics then plays a role), and observing the transmission dynamics on the whole laser beam area (two-dimensional effects are expected). Moreover, working with a 1053 nm wavelength could provide a strong test of the nonlinear multiphoton ionization models and slow down the phase transition. It allows one to better highlight the role of the initial solid state. Another consequence is that the role of hydrodynamics becomes important during the phase transition.

This is the purpose of the present work, where an experiment within such conditions has been carried out and then numerically modeled with hydrocodes that include the solid-to-plasma transition of the ablator in order to perform numerical simulations to further assess the validity of the developed models and to exhibit additional effects pertaining to the initial solid state.

The paper is organized as follows. Section II describes the setup of the experiment, focusing on the various diagnostics used for the analysis of the results. The solid-to-plasma transition model incorporated into the hydrocode used to simulate the experiment is presented in Sec. III. Experimental and simulated results are compared in Sec. IV. Conclusions and outlooks are given in Sec. V.

II. EXPERIMENTAL SETUP

The experiment consisted in illuminating a flat polystyrene target with a thickness of 190 μm by the GCLT (Générateur de Choc Laser Transportable, Transportable Laser Shock Generator) [11], a laser facility that can deliver up to 100 J in 20 ns at 1ω (1.053 μm). The incident laser beam, 48 mm in diameter, is focused, after passing through a random phase plate (RPP), by a plano-convex lens with a focal length of 300 mm in the center of the chamber where the target is placed. The random phase plate after focusing generates a speckle pattern in the far field whose envelope is a super-Gaussian of full width at half-maximum (FWHM) of 500 μm. At the exit of the experiment chamber, in the axis of the laser beam, an achromatic collecting lens with a focal length of 100 mm and an aperture of F/2 allows the light transmitted through the target to be separated into different axes towards four different diagnostics. Two diagnostic systems focus on monitoring energy and power balance, utilizing a calorimeter and a time-resolved diode. The other two systems are dedicated to imaging the transmitted light. To accomplish this, a focusing achromatic lens with a 500 mm focal length and an aperture of F/10 captures the transmitted light, directing it to both triggered ICCD for recording instant images and a streak camera for tracking the temporal evolution of a slice of transmitted light. For a wavelength of 1053 nm, the theoretical diameter of the Airy disk reaching the diagnostics is equal to 24 μm, which is larger than the pixel size of the streak camera (4.4 μm). Additionally, the diameter of the spot, after considering the magnification of the imaging system, is equal to 2500 μm. The setup of the experiment is provided in Fig. 1.

In the experiment presented here, the objective is to observe the transition from solid to plasma, at 1ω. Since this transition is expected to take place at low intensity (10^{11} W/cm^2 [10]), a square pulse of 4 ns and a total energy of 25 J were chosen. Considering the phase plate used, the illumination at the center of the focal spot is then 2.3×10^{12} W/cm^2.

During the campaign, several shots were conducted giving similar results. The spatial and temporal profiles of the laser

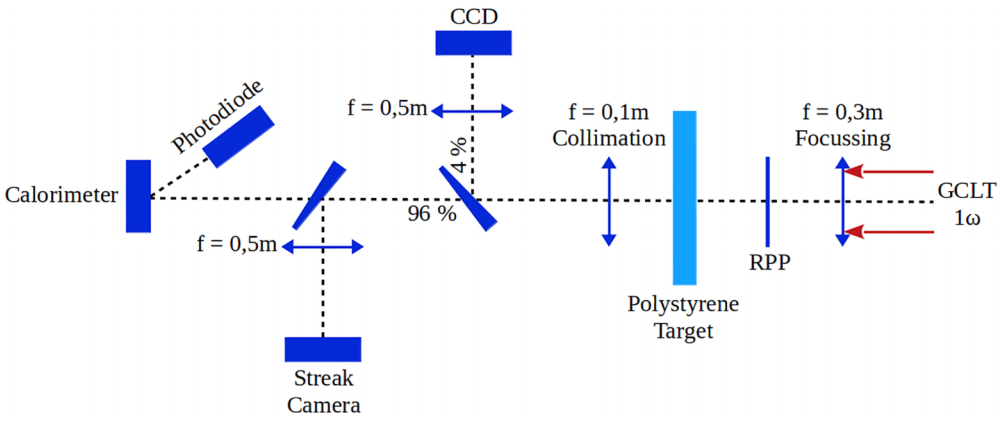

FIG. 1. Experimental setup: The laser is focused on the polystyrene target and passes through the random phase plate to fix the spatial distribution, which is crucial for a reproducible experiment. The transmitted light is then directed to four different diagnostics: an ICCD to record the spatial distribution, a streak camera for the temporal evolution of the distribution, and a calorimeter coupled to a photodiode for the power balance.

intensity coming from one experimental are shown in Fig. 2 for illustration purposes. Figure 2(a) is the spatial intensity distribution recorded on the CCD at low flux without the target. Figure 2(b) is a slice of this spatial distribution along the *y*-axis, passing through the center of the focal spot. The cyan (light gray) curve represents the experimental data, and the dark blue (gray) curve corresponds to the data used for the simulation (refer to Sec. IV). It reveals that the experimental profile is not exactly a super-Gaussian beam: it is a combination of a fifth-order super-Gaussian profile with edges corresponding to a Gaussian shape. This description accounts on average for the experimental shape. Figure 2(c) is the temporal evolution of this intensity at the center of the focal spot. Figure 2(d) illustrates a 2D slice of the laser intensity transmitted through the target as it evolves with respect to time. The decrease in target transmittance at 0.8 ns is

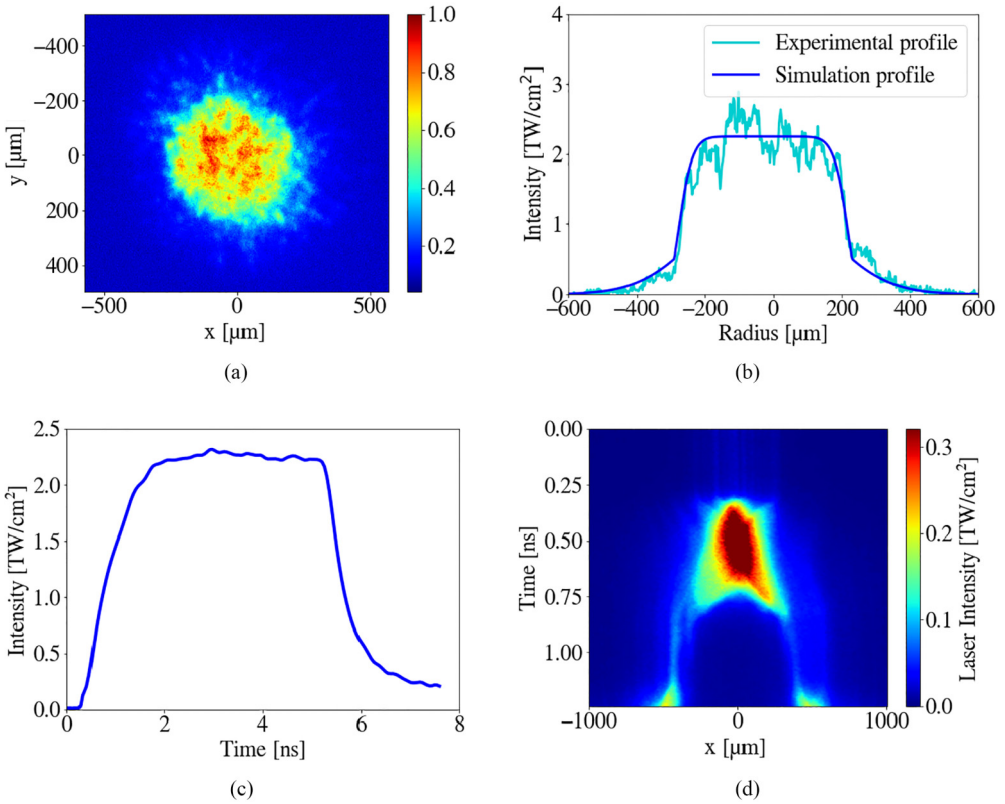

FIG. 2. (a) Spatial distribution of laser intensity at the focal spot. (b) Slice of spatial distribution along the *y*-axis, passing through the center of the focal spot (cyan, light gray), and spatial profile used in simulations (blue, dark gray). (c) Temporal evolution of incident laser intensity at the center of the focal spot. (d) Experimental streak camera image.

due to the solid-to-plasma transition effect, as explained in Sec. IV.

III. MODEL

To simulate the experiment, we used a hydrodynamic code coupled with a new solid-to-plasma transition model. The code is a 3D arbitrary Lagrangian Eulerian (ALE) radiation hydrodynamics code [12]. It resolves the two-temperature multimaterial radiation hydrodynamics using the Lagrangian formalism on an unstructured mesh. The thermal conductivity is modeled using the Hubbard model (degenerate cases) and the Spitzer model, with a harmonic mean across different chemical species. The flux is limited by a sharp cap of 6%. We utilize an EOS developed by LLE to specifically match the evolution of polystyrene during the solid-to-plasma transition. The mesh quality is improved during the run by using ALE methods. The laser propagation and energy deposition in the domain are handled by standard 3D raytracing algorithms, which were modified to include the solid-to-plasma transition as shown below.

The modeling of the solid-to-plasma transition is done by adapting the model describing this transition for polystyrene [9] so that it can meet the specific physical and numerical requirements of our hydrodynamic code. Its primary purpose is to track electronic dynamics, which is used to compute the material's dielectric permittivity. This permittivity is crucial because it provides information about the laser trajectory and energy deposition into the material, which in turn affects the hydrodynamic response.

The ionization model proposed in Ref. [9] accounts for the chemical fragmentation of the ablator that takes place during the transition [8]. As the temperature of polystyrene increases, it undergoes chemical reactions and breaks down into smaller molecules such as styrene, benzene, and acetylene, ultimately transitioning into a fully ionized plasma state. Due to the varying ionization energies of these molecules, it becomes necessary to track the ionization process for each of them. In Ref. [9], all chemical species are tracked in parallel, as well as their different ionization states. Each of these species has a specific population dynamics equation depending on the temperature of the material and the ionization mechanisms. This method enables a precise evaluation of the ionization but is computationally expensive in terms of storage and time.

For computational simplicity, i.e., allowing an efficient coupling with hydrodynamics, the new model assumes that all chemical fragmentations occur instantaneously at two specific lattice/molecule temperatures T_i. These two temperatures were selected because they correspond to the dissociation temperatures of styrene and benzene, respectively [8]. This approximation is based on the fact that, according to [9,13], the timescale of styrene dissociation when the temperature exceeds 2.4 eV is on the order of 10^{-13} s, which is significantly shorter than the hydrodynamic code time step (minimum 10^{-12} s). The same observation stands for benzene at 6 eV. For illustrative purposes, we can consider Fig. 2(a) of [9], which shows the time evolution of the density of styrene, benzene, and carbon-hydrogen plasma during one of their simulations. While our simulation settings differ, the physical principles are comparable. We observe that the kinetics of fragmentation is in the ps timescale. This result is consistent with the dissociation rate and validates our hypothesis.

TABLE I. New chemical fragmentation model: the horizontal arrow represents the evolution of the lattice/molecule temperature of the material T_i. The fragmentation of each chemical species is assumed to be instantaneous at their respective fragmentation temperatures. PS, polystyrene; S, styrene; B, bezene; C, carbon; H, hydrogen; E_I, ionization energy; n_{p0}, density of ionizable electrons; σ, photoionization cross section ($s^{-1}\,m^{-3}[W\,m^{-2}]^{-n}$); n, number of laser photons needed to ionize one valence electron.

	2.4 eV	6 eV	T_i
Chemical species	PS/S	B	CH
E_I (eV)	4.05	9.2	11.3
n_{p0} (cm^{-3})	6.36×10^{21}	6.36×10^{21}	5.73×10^{22}
1ω σ	3.55×10^{-28}	3.97×10^{-101}	1.02×10^{-137}
n	4	8	11

The new model also assumes that only the first ionization for each chemical species is considered. This hypothesis implies that the electron temperature T_e remains lower than the second ionization energies of the species. This is a reasonable assumption because we are working within a context of multipicosecond timescale variations, and the thermalization timescale of the material is subpicosecond at any step of the solid-to-plasma transition [8]. Therefore, T_e is of the same order of magnitude as T_i, which is lower than the first ionization energy E_I for each chemical species, as illustrated in Table I.

In the model of Ref. [9], chemical fragmentation directly affects the ionization energy of a chemical species and its density inside the material, which is equal to the density of ionizable electrons from that species. In the new model, both the ionization energy and the number of ionizable electrons are imposed by the fragmentation step, and consequently by the temperature.

Table I summarizes the new model of chemical fragmentation, including the lattice/molecule temperatures of transition T_i between different chemical species, the evolution of ionization energies (E_I), and the changes in the density of ionizable electrons. It also provides parameters that pertain to the simplified photoionization model discussed later, the photoionization cross section σ, and the number of laser photons needed to ionize one valence electron n.

In Ref. [9], the studies were conducted without hydrodynamics. The objective of the new model is to be incorporated into a hydrodynamic simulation. These simulations employ time steps that are significantly longer than those involved in electron dynamics, ranging from 10^{-12} to 10^{-14} s, in contrast to the electron dynamics time step of 10^{-15} s. Consequently, the ionization calculation is subcycled between two hydrodynamic steps.

The new model requires addressing the evolution of the mass density ρ because it evolves due to hydrodynamics, which was not taken into account in the previous model. In a purely hydrodynamic calculation, the densities of chemical species, including electrons, ions, atoms, or molecules, are directly proportional to the material mass density. This is

expressed for any species k in the equation

$$n_k(t) = n_{k_0} \times \frac{\rho(t)}{\rho_0}. \tag{1}$$

Here, n_k represents the particle density of chemical species k, ρ represents the density of the material, ρ_0 is the selected reference density (throughout this paper, we use $\rho_0 = 1.1\ \mathrm{g\,cm^{-3}}$ to denote the mass density of solid polystyrene), and n_{k_0} denotes the particle density of species k when $\rho = \rho_0$.

However, it is worth noting that some ionization mechanisms exhibit nonlinear dependencies on density, which will be detailed in a subsequent section. This nonlinearity affects both the free-electron density n_e and the valence electron density n_v. Therefore, to account for this nonlinearity, it becomes necessary to follow the hydrodynamic evolution of density and correct n_e at each hydrodynamic time step using the expression $n_e = n_{e_{\mathrm{prev}}} \frac{\rho}{\rho_{\mathrm{prev}}}$, where $n_{e_{\mathrm{prev}}}$ and ρ_{prev} are the free-electron density and mass density before the hydrodynamic update.

Regarding valence electrons, since the model is limited to the first ionizations of each chemical species, n_v can be expressed as a function of n_e and the ionizable chemical species density n_p, which depends on the fragmentation stage (see Table I). Utilizing Eq. (1) for n_p, we derive the following expression for n_v:

$$n_v(t) = n_{p0}(t)\frac{\rho(t)}{\rho_0} - n_e(t). \tag{2}$$

In the model presented in Ref. [9], the dynamics of electrons are driven by three physical mechanisms: photoionization, electron impact ionization, and electron recombination.

Photoionization represents the direct absorption of photons by valence electrons. The number of photons required to ionize one electron depends on the ionization energy (E_I) of the material. In the case of polystyrene, which has an ionization energy of 4.05 eV, a laser beam at 1053 nm requires four photons to ionize one electron. This photoionization process is described in Ref. [9] using Keldysh's model [14]. Electron impact ionization takes into account the collision rate between valence electrons and free electrons with energies exceeding the ionization energy. This process is described by using Gryzinski's theory [9,15]. Lastly, electron recombination is described using Zel'dovich's formula adapted to dense plasmas [16].

In our new model, these three ionization parameters have been adapted to account for hydrodynamic variations and to improve computational efficiency. It employs an approximation formula for the Keldysh photoionization term $\mathrm{W_{PI}}$ that is relevant for the laser intensity range of our study. For the impact ionization, the new model combines Gryzinski's theory with a Maxwell-Boltzmann distribution for electron energies to remove threshold effects. For the electronic recombination term, the new model utilizes the simplified proportionality model employed in [6]. All the details of these modifications are presented in Appendixes A and B.

The final differential equation for the evolution of the free-electron density, which is integrated into the hydrodynamic code, is as follows:

$$\frac{dn_e}{dt} = \sigma I^n \frac{n_{p0}\frac{\rho}{\rho_0} - n_e}{n_{p0}} + \alpha(T_e) n_e \left(n_{p0}\frac{\rho}{\rho_0} - n_e\right) - \nu_{\mathrm{rec}} n_e. \tag{3}$$

Here, σ and n are the two photoionization parameters presented in Table I, I is the laser intensity ($\mathrm{W\,m^{-2}}$), and $\nu_{\mathrm{rec}} = 10^9\ \mathrm{s^{-1}}$ is the recombination frequency. The Keldysh photoionization term $\mathrm{W_{PI}}$ is described in detail in Appendix A and the impact ionization term α is described in Appendix B.

Between two hydrodynamic time steps, all the hydrodynamic and laser parameters in Eq. (3) remain constant over time. This enables us to solve this equation analytically, giving the following expression for the evolution of n_e:

$$n_e = \frac{1}{\left(\frac{1}{n_{e0} - n_{e\text{-lim}}} + \frac{\alpha}{\sqrt{\Delta}}\right)\exp(\sqrt{\Delta}\delta t) - \frac{\alpha}{\sqrt{\Delta}}} + n_{e\text{-lim}}, \tag{4}$$

where

$$\Delta = \left(\alpha n_{p0}\frac{\rho}{\rho_0} - \frac{W_{PI}}{n_{p0}} - \nu_{\mathrm{rec}}\right)^2 + 4\alpha W_{\mathrm{PI}}\frac{\rho}{\rho_0},$$

$$n_{e\text{-lim}} = \frac{1}{2\alpha}\left(\alpha n_{p0}\frac{\rho}{\rho_0} - \frac{W_{PI}}{n_{p0}} - \nu_{\mathrm{rec}} - \sqrt{\Delta}\right).$$

Here, n_{e0} is the free-electron density after the density correction, and δt is the hydrodynamic time step.

The permittivity of a material is a fundamental property that describes the interaction between light and matter. In the context of a solid-to-plasma transition, it is essential to use a permittivity model that accounts for both laser-solid and laser-plasma interactions. The model proposed by Gamaly and Rodes [17] incorporates into the Drude permittivity a term that depends on the density of valence electrons in the material. This term is expressed as

$$\epsilon_v = 1 + (\epsilon_s - 1)\left(1 - \frac{n_e}{n_p}\right), \tag{5}$$

where $\epsilon_s = 2.5$ represents the permittivity of solid polystyrene [18]. This formulation describes the transition from the solid permittivity model to the ideal low-density plasma permittivity model as the material undergoes ionization. It is designed to work at constant mass density because as n_e approaches n_p, ϵ_v approaches 1, representing the behavior of a fully ionized plasma. However, in scenarios where there is no ionization and a decrease in mass density, this formula leads to $\rho \to 0 \Rightarrow n_e \to 0 \Rightarrow \epsilon_v \to \epsilon_s$. This contradicts the fact that low-density matter (such as gas) has a permittivity close to 1. This paradox appears because the variation in mass density is not taken into account in Ref. [17]. Indeed, the term $1 - \frac{n_e}{n_p}$ represents the normalized valence electron density, which is proportional to the mass density of the material. A more physically accurate approach is to define this valence electron permittivity as

$$\epsilon_v = 1 + (\epsilon_s - 1)\left(\frac{\rho}{\rho_0} - \frac{n_e}{n_{p0}}\right). \tag{6}$$

This new formula is equal to the one of Ref. [17] when $\rho = \rho_0$ and maintains consistency with the ideal low-density matter limit. The final formula for permittivity used in our

model is, therefore,

$$\epsilon = 1 + (\epsilon_s - 1)\left(\frac{\rho}{\rho_0} - \frac{n_e}{n_{p0}}\right) - \frac{n_e}{n_c}\left(1 + i\frac{\nu_c}{\omega_0}\right)^{-1}, \quad (7)$$

where n_c is the plasma critical density, ω_0 is the laser frequency, and ν_c is the electron-material collision frequency, which is described in the following paragraph.

The collision frequency used to characterize the absorption of laser energy by electrons changes dramatically during the solid-to-plasma transition. In solid polystyrene, when $T_i <$ 58 meV, energy absorption occurs through collisions between free electrons and phonons. The model for electron-phonon collision frequency in solid polystyrene is developed in [8], based on a more general work [19] about electron-phonon collisions in solids. As polystyrene begins to melt, its periodic structure and the associated phonons disappear. At this point, the material enters the dense plasma domain, where energy absorption is caused by interactions between free electrons and ions, and the Lee and More model for electron-ion collision frequency in dense plasma is used [20]. In our new model, we continue to use the Lee and Moore model for the hot material. However, as detailed in Sec. IV, we have modified the collision frequency model at low temperatures to better account for the experimental results.

This permittivity is used in the laser propagation section of the code. A raytracing algorithm is employed to solve the eikonal equation, which determines the path of light within the material. Additionally, the code uses the imaginary component of the permittivity to calculate the energy deposited by the laser.

IV. RESULTS AND DISCUSSION

We now perform simulations of the GCLT experiment described in Sec. II using the model described in Sec. III and implemented in the 3D hydrodynamics code [12]. We first perform a set of 1D calculations to validate the dynamics of the laser transmission along the axis, and then we study higher-order effects with 3D simulations.

Figure 3 displays the temporal evolution of experimental incident and transmitted intensity at the center of the focal spot. This evolution is primarily governed by the solid-to-plasma transition physics. Initially, at the start of the laser pulse, the polystyrene is transparent, causing the transmitted intensity to closely match the incident one (with approximately 5% specular reflection). As the laser intensity increases, the material becomes more and more absorbing due to the growing density of free electrons. Consequently, the target transmittance, which is the ratio of transmitted to incident intensity, decreases.

The figure also presents a comparison between these experimental results and the transmitted intensity obtained from two 1D simulations. The main difference between the two simulation, represented by Figs. 3(a) and 3(b), is the electron-phonon collision model, as discussed in Sec. III. Figure 3(a) shows the results of the simulation using the frequency model from [8]. This figure indicates that the simulation captures the general physical trends of the transition; the transmitted intensity reaches the correct value, and the transmission ends at the appropriate time. However, there is an issue in the

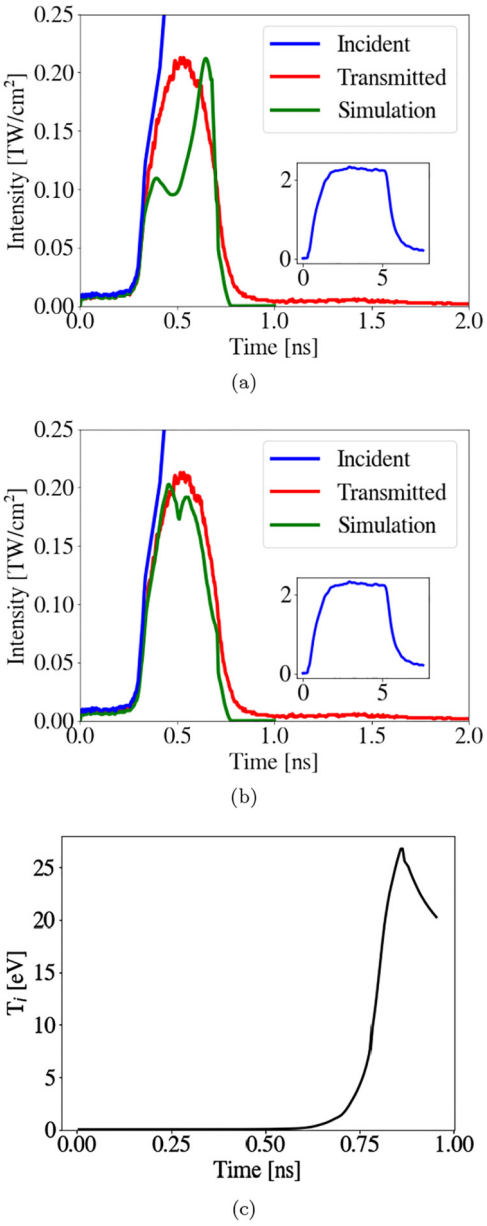

FIG. 3. (a) Comparison between the laser intensity incident (blue, the upper one), the laser intensity transmitted by the polystyrene target at the center of the focal spot (red, the middle one), and the result of a 1D simulation using the electron-phonon collision frequency of the model of Ref. [9] (green, the lowest). (b) Same comparison with the electron-phonon collision frequency set to 6×10^{14} s^{-1}. (c) Evolution of T_i at the center of the focal spot, on the front layer of the target, during the simulation presented in (b).

transmission dynamics around 0.5 ns, indicating irregularity in laser absorption. Two factors could contribute to this fluctuation: the dynamics of electron density or the collision frequency. The electron dynamics is less likely to be the cause because the time at which the plasma becomes reflective, corresponding to when the electronic density reaches the critical density, is accurate in the simulation. On the other hand, the collision frequency can alter absorption without affecting the transmission duration. Additionally, Fig. 3(c) indicates that 0.5 ns is the time when the material temperature begins to rise,

and thus the polystyrene begins to melt. This suggests that the electron-phonon collision frequency value might be too high, leading to excessive laser absorption before 0.5 ns. This hypothesis is not contradictory with the work presented in [10] where the model from [9] was experimentally validated. The 351 nm laser beam increased the material temperature more rapidly, shortening transmission in cold polystyrene compared to the entire pulse, making this effect less noticeable.

The electron-phonon collision model is based on various physical properties of solid polystyrene. Initially, we examined if the combined uncertainties of these parameters could account for a margin of error sufficient to encompass our results. This approach did not justify the required order of magnitude decrease in the collision frequency. As a result, we concluded that the model does not accurately account for the electron-phonon collision frequency under our experimental conditions. That is why we decided to use this collision frequency as a fitting parameter. Figure 3(b) shows the results of the simulation using the fitted electron-phonon collision frequency $\nu_c = 6 \times 10^{14}$ s^{-1}. It is important to note that only the collision frequency of the solid polystyrene has been changed; all the physical processes after 0.5 ns remain the same as those presented in Sec. III.

Another point of discrepancy between the simulation and the experiment, as observed in Fig. 3(b), is a slight dip in transmission that occurs at the peak of the simulated transmission curve. This dip is a consequence of the transition between the electron-phonon collision frequency model of the solid and the electron-ion collision frequency model of the plasma. The electron-ion collision frequency (on the order of 10^{13} s^{-1}) is considerably lower than the electron-phonon collision frequency, leading to a sudden increase in transmission in the code, i.e., less laser absorption.

Figure 3(c) depicts the evolution of T_i at the center of the focal spot, situated on the front layer of the target, throughout the simulation presented in Fig. 3(b). This graph illustrates the short lifespan of benzene molecules during the transition from solid to plasma, occurring between 2.4 and 6 eV, further supporting our model of instantaneous dissociation presented in Sec. III.

Although 1D simulations show reasonable agreement between experimental observations and numerical simulations, it is necessary to perform 3D simulations since they are crucial for studying more complex physical effects, including illumination geometry, scattering, and thermal conduction. Figure 4(a) illustrates the evolution of the polystyrene target at three different times during the laser pulse. The figure displays the laser intensity over one-quarter of the polystyrene target, with each image normalized for clarity, providing insights on the bulk dynamics. Initially, at the beginning of the laser pulse, the target remains fully transparent to the laser. As the time elapses, the front face of the target starts to ionize, leading to an increase of free-electron density up to the critical density. This transition makes the target reflective, as observed at $t = 0.5$ ns. Simultaneously, the laser intensity at the periphery of the focal spot remains insufficient to ionize the polystyrene, resulting in continued laser transmission through the target. Finally, at $t = 1$ ns, the plasma region, characterized by a density of free electrons close to the critical density, exhibits high absorption. This absorption significantly increases the temperature, leading to the expansion of the plasma at the front face of the target.

We can see in Fig. 4(a) that speckles are not modeled in this simulation. We think that modeling of laser speckles using the raytracing approximation is currently not possible within a physically consistent manner, as it would require high-order techniques to reconstruct the interference pattern from the ray phase, which is currently not realistic in large-scale hydrodynamics codes [21]. However, it is possible to include intensity modulations in the laser profiles in order to mimic speckles, but without the diffraction effect. In the simulations, we have instead modeled the intensity profile envelope, which allows coarsening the numerical resolution of the simulation significantly since speckles do not need to be resolved. The data collected in the experiment do not suggest that the transition occurs more rapidly in speckles, which may be due to insufficient resolution of the diagnostic. As a consequence, it does not appear necessary to artificially model the speckles in the hydrodynamics simulation.

To facilitate a direct comparison between the simulation results and the experimental data, it was essential to replicate the available diagnostics. Figure 4(c) provides an illustration of the simulation output in the form of a streak camera image, which can be compared to the experimental image shown in Fig. 4(b). First, the simulation accurately replicates the evolution of transmission at the center of the focal spot, as shown by the observations from the 1D simulations in Fig. 5. This includes the notable drop in transmission that remains visible at the peak of laser intensity. Furthermore, the simulation successfully reproduces the presence of the wings observed in the experimental image. These wings are a 2D visualization of the effect that we described in the analysis of Fig. 4(a). When the laser intensity at the center of the focal spot becomes so high that the plasma becomes reflective, the intensity can no longer be measured at the center of the target. However, the outer part of the hyper-Gaussian laser beam never reaches this high intensity and continues to be measured by the streak camera during the whole pulse duration.

However, when closely examining the two images, clear distinctions emerge. Particularly, the transverse profiles of the two images display noticeable differences. Figure 4(d) illustrates the profiles of the two images at 0.5 ns. In this figure, we observe that the simulated profile has not changed much at this point, which accounts for the fact that the laser intensity at this time is not high enough to ionize the polystyrene. However, the experimental profile does not correspond to the incident one. Similarly, when considering the profile of the streak camera image at 1.2 ns, as shown in Fig. 4(e), it appears broader than the simulated profile.

Several hypotheses can potentially explain these differences. The streak camera image profile at 0.5 ns might be due to saturation during data acquisition. It could also be due to focusing effects caused by an increase in free electrons in the front surface of the target. Diffraction effects might also explain the observed broadening of the experimental signal at 1.2 ns. Indeed, as the plasma at the front surface of the target starts to expand, as seen in Fig. 4(a), it creates an optical index gradient. This gradient can lead to lateral refraction, which can change the trajectory of the laser beam and change the position of the wings. Unfortunately, this gradient is too

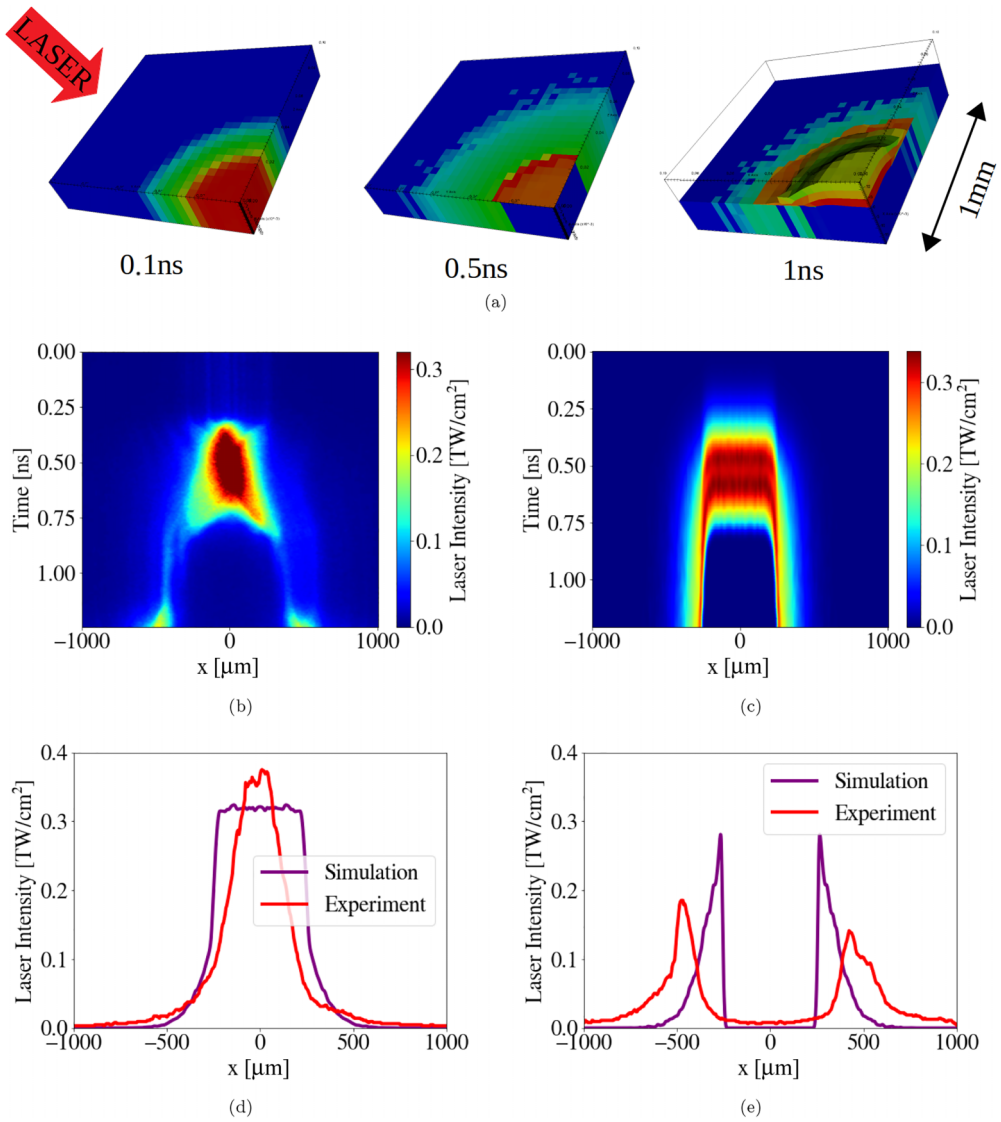

FIG. 4. (a) 3D representation of the laser intensity arriving on a polystyrene target at three times of the laser pulse. (b) Experimental streak camera image. (c) Simulated streak camera image. (d) and (e) Comparisons of spatial laser intensity profiles of experimental and simulated streak camera images at 0.5 and 1.2 ns, respectively.

pronounced for the current lateral resolution of the hydrodynamic mesh, resulting in a difference between calculated diffraction and experimental results. Indeed, the refractive index within each cell is averaged, which decreases the effect of refraction, a nonlinear effect. Attempting to mitigate this issue by reducing the mesh cell size is technically difficult with our current code, as is shown in Appendix C, but it could become possible in the future.

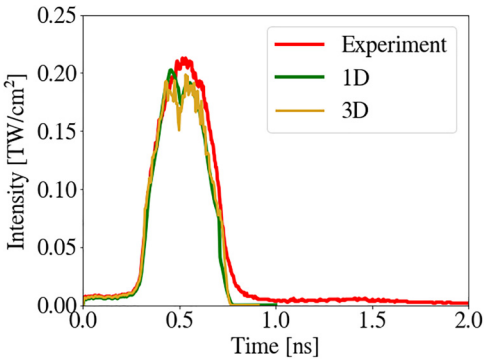

FIG. 5. Comparison of transmitted laser intensity between the 1D simulation and the center of the 3D simulation.

Finally, it is important to study the effect of possible inaccuracy in the theoretical model. Throughout our analysis of the experimental results, numerous 3D simulations were conducted to understand the influence of the model physical parameters on the simulation outcomes. The parameters related to electron dynamics and absorption physics influence the evolution of longitudinal absorption, as illustrated in Fig. 3. However, they do not significantly alter the transversal shape of absorption observed in Figs. 4(d) and 4(e). The fact that modifications to the nonlinear dynamics of absorption in the material do not change its transversal shape strongly supports the hypothesis of insufficient spatial resolution. Another set of parameters that could have an influence on the

simulation is the equation of states used for our hydrodynamic simulation. Unfortunately, we had only one EOS working for the polystyrene in our operating area, coming from work made at the LLE. So it was not possible to verify whether the EOS may change the numerical results or not. Overall, it is worth noting that slight variations of the parameters used leave the main conclusions of the present work unchanged, which suggests the reliability of our approach.

V. CONCLUSION AND PERSPECTIVES

In conclusion, this work continues the development of the solid-to-plasma transition model from Ref. [9], experimentally benchmarked in Ref. [10]. The experiment carried out on the GCLT facility was a new opportunity to test the model at a new wavelength and in a configuration where hydrodynamics effects have to be taken into account in a simulation. To achieve this, the model has been adapted to accommodate the physical and computational constraints of a hydrodynamic code, considering the evolving hydrodynamic parameters and introducing precise simplifications to reduce computational complexity. It has then been coupled with a 3D hydrodynamics code, including a 3D raytracing package. The comparison between experimental results and simulations assesses the validity of the solid-to-plasma transition model and its coupling to a hydrocode. This work provides a second verification of the solid-to-plasma transition model with experiments, complementary with the benchmark, allowing this model to be used to simulate more complex experiments, particularly in the context of inertial confinement fusion simulations.

To further progress in this topic, it might be important to find a better way to model the electron-phonon collision frequency in solid polystyrene so that it can account for the experimental results without fitting parameters. It might also be interesting to add more diagnostics to the solid-to-plasma transition experiment. For example, employing interferometric diagnostics to measure the frequency shift generated by the temporal evolution of the refractive index would provide additional information about the spatial distribution inside the polystyrene layer, along with the measurement of absorption.

ACKNOWLEDGMENTS

This material is based upon work supported by the Department of Energy (National Nuclear Security Administration) University of Rochester "National Inertial Confinement Program" under Award No. DE-NA0004144. Access was granted to the HPC resources of TGCC under the allocation 2020-A0070506129 and 2021-A0090506129 made by GENCI. This work was carried out within the framework of the EUROfusion Consortium, funded by the European Union via the Euratom Research and Training Programme (Grant Agreement No. 101052200 – EUROfusion). The views and opinions expressed are, however, those of the author(s) only and do not necessarily reflect those of the European Union or the European Commission. The involved teams have operated within the framework of the Enabling Research Project: ENR-IFE.01.CEA "Advancing shock ignition for direct-drive inertial fusion." An anonymous referee is acknowledged for his/her suggestion of possible perspective for the present work (last paragraph of the Conclusion section).

This report was prepared as an account of work sponsored by an agency of the U.S. Government. Neither the U.S. Government nor any agency thereof, nor any of their employees, makes any warranty, express or implied, for the accuracy, completeness, or usefulness of any information, apparatus, product, or process disclosed, or represents that its use would not infringe privately owned rights. Reference herein to any specific commercial product, process, or service by trade name, trademark, manufacturer, or otherwise does not necessarily constitute or imply its endorsement, recommendation, or favoring by the U.S. Government or any agency thereof. The views and opinions of authors expressed herein do not necessarily state or reflect those of the U.S. Government or any agency thereof.

APPENDIX A: ADAPTATION OF PHOTOIONIZATION MODEL

The Keldysh photoionization model [14] used in Ref. [9] is highly accurate but computationally intensive due to the numerous integrals involved. Consequently, our new model utilizes an approximation formula to calculate the Keldysh photoionization term: $W_{\mathrm{PI}} = \sigma I^n$, where σ is the generalized multiphoton absorption cross section, which depends on E_I, and n is the number of laser photons needed to ionize one valence electron [6,22]. This formulation offers a precise approximation for the range of laser intensities relevant to our study, spanning from 10^9 to 10^{12} W cm^{-2} (where multiphoton absorption is the main process, i.e., tunneling is negligible). The values of these two parameters are provided in Table I for each chemical fragmentation stage and for laser beams at 1ω.

This photoionization rate is then adjusted by the ratio between the density of valence electrons available for ionization and the density of ionizable chemical species at solid density, n_{p0}. This correction is essential because W_{PI} is defined for a weakly ionized solid. Therefore, the photoionization term can be expressed as

$$\left.\frac{dn_e}{dt}\right|_{\text{photoionization}} = \sigma I^n \frac{n_{p0}\frac{\rho}{\rho_0} - n_e}{n_{p0}}. \tag{A1}$$

APPENDIX B: INTEGRATION OF THE MAXWELL-BOLTZMANN DISTRIBUTION IN THE ELECTRON IMPACT IONIZATION MODEL

In Ref. [9], the electron impact ionization rate is calculated considering that all free electrons are at the same temperature. This hypothesis creates a threshold effect in the ionization rate because in that case electron impact ionization can only occur when the global electron temperature is higher than the ionization energy of the material. This threshold effect creates discontinuities in the free-electron density, leading to numerical instabilities in the hydrodynamic code. To overcome this problem, the new model uses the Maxwell-Boltzmann distribution for the free-electron energy distribution, as described in the next paragraph [1,17,23–29].

The collision rate between a valence electron and a free electron of a specific energy E, denoted as α_{1e} (m^3 s^{-1}), is

determined using Gryzinski's theory [15], as it is in Ref. [9]:

$$\alpha_{1e}(E) = 4\sigma_B F\left(\frac{3}{2}\frac{E}{E_I}\right)\sqrt{\frac{8E}{\pi m_e}}, \tag{B1}$$

where

$$F(x) = \frac{10(x-1)}{\pi x(x+8)} \text{ and } \sigma_B = 0.88 \times 10^{-16}\ \text{cm}^2.$$

Then the number of free electrons with a given energy E, $dn_{e_E}(T_e)$, is computed using the Maxwell-Boltzmann distribution:

$$dn_{e_E}(T_e) = n_e \frac{e^{-\frac{E}{k_B T_e}} dE}{\int_0^\infty e^{-\frac{\epsilon}{k_B T_e}} d\epsilon}. \tag{B2}$$

By combining these two equations, we can calculate the ionizing collision frequency per valence electron ν_{ii} (s^{-1}) as follows:

$$\begin{aligned}\nu_{ii} &= \int_{E_I}^\infty \alpha_{1e}(E)\, dn_{e_E}(T_e) \\ &= \int_{E_I}^\infty 4\sigma_B F\left(\frac{3}{2}\frac{E}{E_I}\right)\sqrt{\frac{8E}{\pi m_e}}\, n_e \frac{e^{-\frac{E}{k_B T_e}} dE}{\int_0^\infty e^{-\frac{\epsilon}{k_B T_e}} d\epsilon} \\ &= \alpha(T_e)\, n_e,\end{aligned} \tag{B3}$$

where

$$\alpha(T_e) = \frac{\int_{E_I}^\infty 4\sigma_B F\left(\frac{3}{2}\frac{E}{E_I}\right)\sqrt{\frac{8E}{\pi m_e}}\, e^{-\frac{E}{k_B T_e}} dE}{\int_0^\infty e^{-\frac{\epsilon}{k_B T_e}} d\epsilon}. \tag{B4}$$

Here, $\alpha(T_e)$ $(\text{m}^3\,\text{s}^{-1})$ represents the average ionizing collision frequency of a free electron with a valence electron.

APPENDIX C: REDUCTION OF THE HYDRODYNAMIC MESH CELL SIZE

Reducing the mesh cell size of the hydrodynamic code is technically difficult with our current code. Indeed, the solid-to-plasma transition model relies in part on an estimation of the laser field in the target, which itself is estimated from the ray properties in the mesh. In the current implementation, we use a rigid-binning estimator that uses the ray statistics in each cell to determine the average field in the cell. This estimator is noisy by definition, and requires a good ray statistics. Unfortunately, we have found that to capture correctly the dynamics of the transition, especially when the ionization increases rapidly, we would require a high ray statistics. Our calculations were run at the limit of our current computational capabilities. Better resolving the lateral gradients requires adding at least a factor of 2 to 4 more cells in each lateral direction, which would increase the number of rays required too much. The solution to this problem is to change the ray field estimator to one that generates less noise. This work has been started but is not currently mature enough.

[1] R. Craxton, K. Anderson, T. Boehly, V. Goncharov, D. Harding, J. Knauer, M. McCrory, P. McKenty, D. Meyerhofer, J. Myatt, A. Schmitt, J. Sethian, R. Short, S. Skupsky, W. Theobald, W. Kruer, K. Tanaka, R. Betti, T. Collins, J. Delettrez *et al.*, Phys. Plasmas **22**, 110501 (2015).

[2] S. Atzeni and J. M.- ter- Vehn, *The Physics of Inertial Fusion* (Oxford University Press, Oxford, 2004).

[3] R. Ishizaki and K. Nishihara, Phys. Rev. Lett. **78**, 1920 (1997).

[4] J. L. Peebles, S. X. Hu, W. Theobald, V. N. Goncharov, N. Whiting, P. M. Celliers, S. J. Ali, G. Duchateau, E. M. Campbell, T. R. Boehly, and S. P. Regan, Phys. Rev. E **99**, 063208 (2019).

[5] J. Oh, A. J. Schmitt, M. Karasik, and S. P. Obenschain, Phys. Plasmas **28**, 032704 (2021).

[6] G. Duchateau, S. X. Hu, A. Pineau, A. Kar, B. Chimier, A. Casner, V. Tikhonchuk, V. N. Goncharov, P. B. Radha, and E. M. Campbell, Phys. Rev. E **100**, 033201 (2019).

[7] A. Kar, S. X. Hu, G. Duchateau, J. Carroll-Nellenback, and P. B. Radha, Phys. Rev. E **101**, 063202 (2020).

[8] A. Pineau, B. Chimier, S. X. Hu, and G. Duchateau, Phys. Plasmas **27**, 092703 (2020).

[9] A. Pineau, B. Chimier, S. X. Hu, and G. Duchateau, Phys. Rev. E **104**, 015210 (2021).

[10] A. Pineau, K. R. P. Kafka, S. G. Demos, T. Z. Kosc, V. N. Goncharov, S. X. Hu, and G. Duchateau, Phys. Rev. Res. **4**, 033178 (2022).

[11] T. Géral, E. Lescoute, B. Jodar, and A. Sollier, GCLT: a versatile high power laser facility for high-energy-density (HED) physics applications, *23rd Biennial Conference of the APS Topical Group on Shock Compression of Condensed Matter*, Vol. 68 (Chicago, Illinois, 2023).

[12] A. Colaïtis (unpublished).

[13] M. Chergui, *Femtochemistry, Ultrafast Chemical and Physical Processes on Molecular Systems* (World Scientific, Singapore, 1995).

[14] L. V. Keldysh, Sov. Phys. JETP **20**, 1307 (1965).

[15] M. Gryzinski, Phys. Rev. **138**, A336 (1965).

[16] Y. B. Zel'dovich and Y. P. Raizer, in *Physics of Shock Waves and High-Temperature Hydrodynamic Phenomena*, edited by W. D. Hayes and R. F. Probstein (Dover Publications, Inc. Mineola, New York, 1966).

[17] E. G. Gamaly and A. V. Rode, J. Opt. Soc. Am. B **31**, C36 (2014).

[18] J. E. Mark, *Polymer Data Handbook* (Oxford University Press, Oxford, 1999).

[19] M. V. Fischetti, D. J. DiMaria, S. D. Brorson, T. N. Theis, and J. R. Kirtley, Phys. Rev. B **31**, 8124 (1985).

[20] Y. Lee and R. More, Phys. Fluids **27**, 1273 (1984).

[21] A. Colaïtis, J. P. Palastro, R. K. Follet, I. V. Igumenschev, and V. Goncharov, Phys. Plasmas **26**, 032301 (2019).

[22] C. G. Morgan, Rep. Prog. Phys. **38**, 621 (1975).

[23] J. Nuckolls, L. Wood, A. Thiessen, and G. Zimmerman, Nature (London) **239**, 139 (1972).

[24] D. D. Meyerhofer, R. L. McCrory, R. Betti, T. R. Boehly, D. T. Casey, T. J. B. Collins, R. S. Craxton, J. A. Delettrez, D. H. Edgell, R. Epstein, K. A. Fletcher, J. A. Frenje, Y. Y. Glebov, V. N. Goncharov, D. R. Harding, S. X. Hu, I. V. Igumenshchev, J. P. Knauer, C. K. Li, J. A. Marozas *et al.*, Nucl. Fusion **51**, 053010 (2011).

[25] V. N. Goncharov, T. C. Sangster, R. Betti, T. R. Boehly, M. J. Bonino, T. J. B. Collins, R. S. Craxton, J. A. Delettrez, D. H. Edgell, R. Epstein, R. K. Follett, C. J. Forrest, D. H. Froula, V. Y. Glebov, D. R. Harding, R. J. Henchen, S. X. Hu, I. V. Igumenshchev, R. Janezic, J. H. Kelly *et al.*, Phys. Plasmas **21**, 056315 (2014).

[26] S. Bodner, Phys. Rev. Lett. **33**, 761 (1974).

[27] P. B. Radha, V. N. Goncharov, T. J. B. Collins, J. A. Delettrez, Y. Elbaz, V. Y. Glebov, R. L. Keck, D. E. Keller, J. P. Knauer, J. A. Marozas, F. J. Marshall, P. McKenty, D. D. Meyerhofer, S. P. Regan, T. C. Sangster, D. Shvarts, S. Skupsky, Y. Srebro, R. P. J. Town, and C. Stoeckl, Phys. Plasmas **12**, 032702 (2005).

[28] S. X. Hu, P. B. Radha, J. A. Marozas, R. Betti, T. J. B. Collins, R. S. Craxton, J. A. Delettrez, D. H. Edgell, R. Epstein, V. N. Goncharov, I. V. Igumenshchev, F. J. Marshall, R. L. McCrory, D. D. Meyerhofer, S. P. Regan, T. C. Sangster, S. Skupsky, V. A. Smalyuk, Y. Elbaz, and D. Shvarts, Phys. Plasmas **16**, 112706 (2009).

[29] B. M. Smirnov, *Theory of Gas Discharge Plasma*, Springer Series on Atomic, Optical, and Plasma Physics (Springer, New York, 2015).